Microstructure and magnetic properties of the ferromagnetic semiconductor $Ge_{1-x}Mn_x$ following rapid thermal annealing

Zhicheng Xie,[1,2] Gengchen Meng,[1,2] Lianjun Wen,[1] Zhiyuan Zhao,[1,2] Hongli Sun,[1,2] Hongrui Qin,[1,2] Dong Pan,[1,2] Hailong Wang,[1,2] Dahai Wei,[1,2,*] and Jianhua Zhao[1,2]

[1]*State Key Laboratory for Superlattices and Microstructures, Institute of Semiconductors, Chinese Academy of Sciences, Beijing 100083, China*

[2]*Center of Materials Science and Optoelectronics Engineering, University of Chinese Academy of Sciences, Beijing 100190, China*

(Received 10 October 2023; accepted 18 December 2023; published 9 January 2024)

The group-IV $Ge_{1-x}Mn_x$ ferromagnetic semiconductor (FMS) has attracted much interest in spintronics due to its compatibility with semiconductor technology. However, $Ge_{1-x}Mn_x$ FMS prepared at high growth temperature (T_S) meets dilemmas in balancing solubility and intermetallic precipitates, limiting its Curie temperature (T_C) and electrical tunability. In this study, $Ge_{1-x}Mn_x$ films were prepared by magnetron sputtering at low T_S combined with rapid thermal annealing (RTA). We conducted a systematic study of the microstructure, valence state, and magnetic properties of $Ge_{1-x}Mn_x$ films. The phase diagram of $Ge_{1-x}Mn_x$ films versus Mn composition x and RTA temperature T_R was plotted, and face-centered cubic structure $Ge_{1-x}Mn_x$ FMS was achieved with x up to 0.1. As x increased, the hole-mediated ferromagnetism of $Ge_{1-x}Mn_x$ FMS was enhanced, with the T_C reaching 282 K at $x = 0.07$. We found that the magnetoresistance ratio of $Ge_{1-x}Mn_x$ FMS was significantly smaller than that of $Ge_{1-x}Mn_x$ with intermetallic precipitates by two orders, providing an easy method to confirm $Ge_{1-x}Mn_x$ FMS without intermetallic precipitates. Finally, the mechanism of suppressing the formation of intermetallic compounds by RTA is discussed. Our work extends the preparation window for high-quality $Ge_{1-x}Mn_x$ FMS, and also provides a promising choice for further investigation of ferromagnetic semiconductors.

DOI: 10.1103/PhysRevB.109.024407

I. INTRODUCTION

In the past several decades, ferromagnetic semiconductors (FMSs) have attracted significant interest due to the unique combination of semiconductors and long-range ferromagnetism, leading to the potential for spin-based device application [1]. Benefiting from the development of molecular-beam epitaxy (MBE), previous studies have mainly focused on Mn-doped group III-V [2–5] and II-VI [6,7] semiconductors. For example, the Curie temperature (T_C) of (Ga, Mn)As with hole-mediated ferromagnetism [8,9] has been enhanced to 200 K [3], and even full spin-orbit torque switching has been achieved in single-layer (Ga, Mn)As [10]. Recently, (Ga, Mn)As have also played an important role in detecting spin polarization in chiral molecular spin valve devices [11]. However, the quality of (Ga, Mn)As prepared on Si substrates is relatively poor, with T_C as low as 48 K [12]. Therefore, the practical applications of FMSs are still limited by the low T_C and difficulty in integrating into mainstream semiconductor materials.

In contrast, the group-IV $Ge_{1-x}Mn_x$ FMS is a promising candidate, due to the potential for higher T_C and its good compatibility with semiconductor technology [13,14]. The initial study showed a linearly increasing T_C up to 116 K with Mn composition x of 0.035 in hole-mediated $Ge_{1-x}Mn_x$ FMS [13]. Further improvement has been achieved through codoping with Co and Mn [15,16], as well as engineering self-organized nanostructures such as nanocolumns [17,18] and quantum dots [19]. Usually, the microstructures dominate the magnetic properties of FMSs, which is related to the incorporation of transition-metal (TM) atoms (Mn, Fe, and Co *et al.*) into the semiconductor host. However, it is always easy for secondary phase to appear in FMSs, which is difficult to be electrically controlled in devices. For example, $Ge_{1-x}Mn_x$ FMS were usually prepared by MBE at high growth temperature (T_S), which exhibits dilemmas in balancing solubility and intermetallic precipitates [13,20]. The study by Bougeard *et al.* indicated that T_S above 60 °C would promote the formation of intermetallic precipitates such as Ge_3Mn_5 and Ge_8Mn_{11} [21]. Therefore, the properties of $Ge_{1-x}Mn_x$ FMS prepared at high T_S have been limited by low doping composition and intermetallic precipitates, which seems to go against further progress.

Depositing $Ge_{1-x}Mn_x$ films at higher T_S, Mn atoms will have higher energy to migrate over a larger range on a surface. In addition, Mn atoms are more likely to overcome the energy barrier to form compounds. These results make it easier for Mn atoms with enrichment characteristics to generate intermetallic precipitates while growing $Ge_{1-x}Mn_x$ FMS. Especially for the Ge-Mn system, there are various secondary phases [22]. Therefore, depositing $Ge_{1-x}Mn_x$ films at low T_S combined with a key high-temperature nonequilibrium rapid thermal annealing (RTA) treatment is a promising method [23]. The low T_S ensures a more uniform distribution of Mn atoms and avoids the formation of intermetallic

*dhwei@semi.ac.cn

 ©2024 American Physical Society

precipitates in $Ge_{1-x}Mn_x$ films. The subsequent RTA promoted the crystallization of $Ge_{1-x}Mn_x$ films and the incorporation of Mn atoms into the Ge host. The Mn atoms localized in Ge film can be easily doped into the Ge host at high RTA temperature (T_R). However, the Mn atoms in Ge film are not easy to get near other Mn atoms and form intermetallic compounds compared to Mn atoms deposited directly at high T_S. This method has great advantages in the suppression of phase separation. The Mn-doped SiGe FMS prepared by this kind of method has been reported recently, which is free of phase separation and has a higher T_C at the Mn composition x of 0.05 compared with the previous study [13]. Obviously, depositing films at low T_S combined with RTA indeed has the potential to prepare high T_C FMSs without intermetallic precipitates [23].

In this study, $Ge_{1-x}Mn_x$ FMSs were prepared by industrial-friendly magnetron sputtering at 50 °C combined with high-temperature nonequilibrium RTA treatment. Detailed sample structure analyses were performed to understand the structure, distribution, and doping features of Mn atoms in the Ge host with x. We obtained the phase diagram of $Ge_{1-x}Mn_x$ films versus x and T_R, and face-centered cubic (fcc) structure $Ge_{1-x}Mn_x$ FMS can be achieved with x up to 0.1. The intermetallic precipitates have been avoided, which is due to the low T_S. Subsequently, we have investigated the magnetic properties of $Ge_{1-x}Mn_x$ FMS, with T_C reaching up to 282 K at $x = 0.07$. The electrical transport characteristics of $Ge_{1-x}Mn_x$ films were carefully compared, which showed the distinct features of the different microstructures in $Ge_{1-x}Mn_x$ FMS and $Ge_{1-x}Mn_x$ with intermetallic precipitates. Finally, we discussed the mechanism of avoiding intermetallic precipitates in preparing $Ge_{1-x}Mn_x$ FMS by depositing film at low T_S combined with RTA treatment.

II. SAMPLE PREPARATION AND DESCRIPTION

For this study, a series of $Ge_{1-x}Mn_x$ films was grown on intrinsic Ge (100) substrates by magnetron sputtering with a base pressure of 9×10^{-9} Torr. The $Ge_{1-x}Mn_x$ films were grown via a codeposition of Ge and Mn, with x varying from 0.008 to 0.32 at different combinations of powers for each target. Before loading into the growth chamber, the Ge substrate was cleaned using a standard HF/H_2O chemical etching. After thermal desorption of the Ge substrate surface oxide at 800 °C, a flat 50-nm Ge buffer layer was grown on the substrate at 750 °C. The 100-nm $Ge_{1-x}Mn_x$ layer was grown at 50 °C, avoiding intermetallic precipitates [21]. Then, a 5-nm Ge capping layer was deposited at 50 °C. Finally, to promote crystallization and activate Mn dopants, a key nonequilibrium RTA treatment was performed at 800 °C for 30 s in N_2 atmosphere [23]. N_2 cannot react with the 5-nm Ge capping layer, even if they are heated together at 600 ∼ 1200 °C for several days [24]. If there is no additional description, the films mentioned in this work are prepared according to the above conditions. The Mn composition x and layer thickness were measured by energy-dispersive x-ray spectroscopy (EDS) in the scanning electron microscope and atomic force microscopy, respectively. These films were further patterned into 10×40 μm^2 Hall bar devices using photolithography and ion milling. All magnetic measurements were performed by the superconducting quantum interference device (MPMS-3). The electrical transport measurements were performed by a Quantum Design physical property measurement system (PPMS-9T).

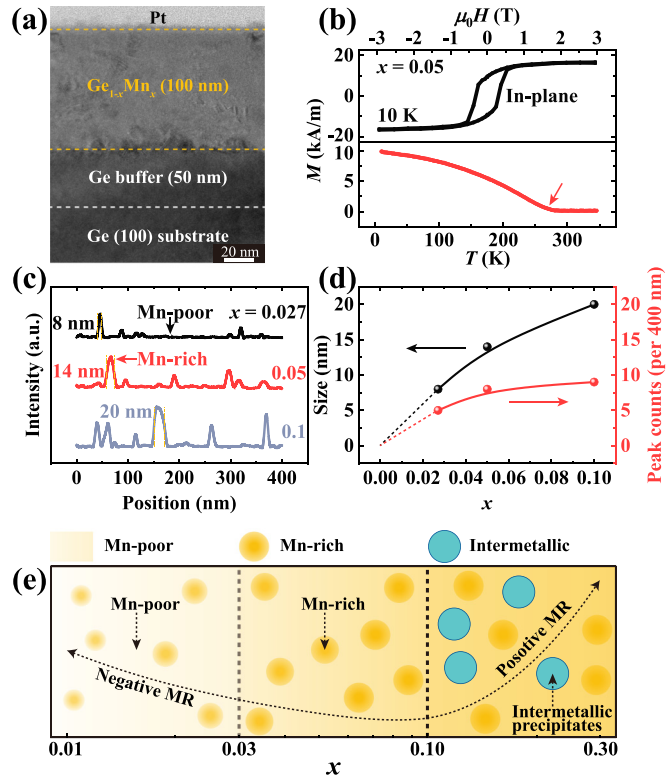

FIG. 1. (a) The cross-sectional TEM image of $Ge_{1-x}Mn_x$ film with $x = 0.05$. (b) The typical in-plane hysteresis loop and magnetization vs temperature curve of $Ge_{1-x}Mn_x$ film with $x = 0.05$. (c) The EDS line scans parallel to the film at $x = 0.027$, 0.05, and 0.1. (d) The x dependence of the FWHM size and peak counts per 400 nm. (e) The schematic diagram of Mn dopants distribution varying with x. The curved dashed line with arrows indicates that the MR of $Ge_{1-x}Mn_x$ films changes from negative MR to enhanced positive MR with x.

The typical cross-sectional transmission electron microscope (TEM) image of $Ge_{1-x}Mn_x$ film is shown in Fig. 1(a). The top is the Pt deposited during the sample fabrication by focused ion-beam etching. Then there is the 100-nm $Ge_{1-x}Mn_x$ layer, where we do not find the existence of intermetallic precipitates. A detailed microstructural analysis will be conducted in the following. The 100-nm $Ge_{1-x}Mn_x$ layer can be easily distinguished compared to the 50-nm Ge buffer layer. Figure 1(b) shows the typical in-plane hysteresis loop at 10 K of $Ge_{1-x}Mn_x$ film with $x = 0.05$. The coercive field ($\mu_0 H_C$) is ≈ 310 mT. T_C is 266 K extracted from the differentiation of magnetization vs temperature curve [25,26]; see the Supplemental Material [27]. Therefore, the $Ge_{1-x}Mn_x$ layer exhibits long-range ferromagnetism, as indicated by this significant magnetic hysteresis, which will be further discussed in Sec. III B.

Usually, Mn atoms as dopants are easily enriched, which will lead to the nonuniform distribution of Mn atoms in the host [17,28]. Therefore, to determine the distribution of Mn atoms in $Ge_{1-x}Mn_x$ films, careful EDS line scans

in TEM were performed parallel to the film, as shown in Fig. 1(c). The EDS intensity of Mn atoms varying with position is nonuniform with fluctuations, which indicates that the distribution of Mn atoms is indeed nonuniform. The EDS intensity also increases as x increases. These peaks and plateaus represent Mn-rich and Mn-poor regions in the host consistent with previous literature [17,28]. The largest size of full width at half maximum (FWHM) is 8, 14, and 20 nm at $x = 0.027$, 0.05, and 0.1, respectively. As shown in Fig. 1(d), the largest size of FWHM increases with x, which indicates that the size of Mn-rich regions in $Ge_{1-x}Mn_x$ films becomes larger with x. The peak counts per 400 nm also increase with x. Therefore, the increasing Mn composition x makes the density of Mn-rich regions in $Ge_{1-x}Mn_x$ films increase. Although the EDS line scans might not be quantitatively accurate, qualitative analysis is sufficient.

Based on EDS line scans and subsequent results, we believe that the distribution of Mn atoms in $Ge_{1-x}Mn_x$ films should be as illustrated in Fig. 1(e). For $Ge_{1-x}Mn_x$ films with low $x(x \leqslant 0.03)$, there should be few Mn dopants in Mn-poor region. Mn dopants are enriched in Mn-rich region. As $x(0.03 < x \leqslant 0.1)$ increases, not only the size and density of Mn-rich regions in $Ge_{1-x}Mn_x$ films increase, but also the Mn dopants in both Mn-poor and Mn-rich regions increase. When x exceeds 0.1, intermetallic precipitates will occur in $Ge_{1-x}Mn_x$ films inevitably. The curved dashed line with arrows illustrates the x dependence of magnetoresistance (MR) characteristics of $Ge_{1-x}Mn_x$ films, which will be discussed later.

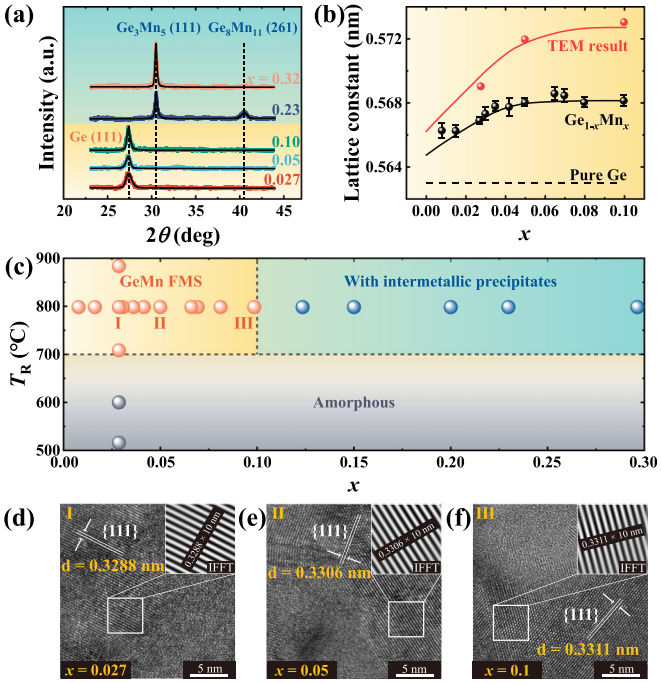

FIG. 2. (a) The XRD patterns of $Ge_{1-x}Mn_x$ films at different x. (b) The x dependence of a extracted by XRD and HRTEM, respectively. (c) The phase diagram of $Ge_{1-x}Mn_x$ films vs x and T_R. The HRTEM images and $d_{\{111\}}$ of $Ge_{1-x}Mn_x$ FMS at (d) $x = 0.027$, (e) $x = 0.05$, and (f) $x = 0.1$, respectively.

III. RESULTS AND DISCSSUSION

A. Sample microstructure characterization

The ferromagnetism of FMSs is related to their microstructures. For typical Mn-doped group III-V and -IV semiconductors, ferromagnetism is hole mediated after Mn atoms are doped into the host [3,13]. During the doping process, the formation of other microstructures might occur. In the Ge-Mn system, there are various microstructures typically such as Ge_3Mn_5 and Ge_8Mn_{11}[22]. Therefore, it is necessary to know the microstructure of our $Ge_{1-x}Mn_x$ films. To get an understanding of the microstructure, x-ray diffraction (XRD) was performed for all $Ge_{1-x}Mn_x$ films. The XRD patterns of Fig. 2(a) show that only Ge (111) of fcc structure appears at $2\theta \approx 27.3^\circ$ with $x \leqslant 0.1$. The Mn atoms did not form secondary phases and were incorporated into the Ge host. The $Ge_{1-x}Mn_x$ films maintain the fcc structure of Ge. However, Ge_3Mn_5 (111) and Ge_8Mn_{11}(261) appear at $2\theta \approx 30.6^\circ$ and $2\theta \approx 40.7^\circ$ with $x > 0.1$, respectively. Obviously, the large x causes the appearance of intermetallic precipitates. The lattice constant (a) increases with x, which was roughly extracted by the Bragg formula for $Ge_{1-x}Mn_x$ films with $x \leqslant 0.1$, as shown in Fig. 2(b). The a is greater than that of fcc Ge [29]. These results are qualitatively consistent with the subsequent TEM analysis. When Mn atoms are doped into the Ge host, the Ge lattice is strained. Because the radius of Mn is larger than that of Ge, Mn will cause the Ge lattice to expand [30].

For our $Ge_{1-x}Mn_x$ films, the microstructure will be greatly influenced by T_R. Therefore, the XRD of $Ge_{1-x}Mn_x$ film at different T_R was performed (Fig. S2(a) [27]). When $T_R < 700$ °C, there are no peaks, and $Ge_{1-x}Mn_x$ films are amorphous. Once $T_R \geqslant 700$ °C, Ge (111) appears, because the RTA treatment promotes the crystallization of $Ge_{1-x}Mn_x$ films. Subsequently, a phase diagram of $Ge_{1-x}Mn_x$ films versus x and T_R was plotted based on the above results, as shown in Fig. 2(c). We name $Ge_{1-x}Mn_x$ films in the yellow, blue, and gray areas as $Ge_{1-x}Mn_x$ FMS, $Ge_{1-x}Mn_x$ with intermetallic precipitates, and amorphous $Ge_{1-x}Mn_x$, respectively. We also noticed that intermetallic precipitates will appear in films once T_S reaches 200 °C (Fig. S2(b) [27]). Compared to high T_R, high T_S is indeed much easier to promote the formation of intermetallic precipitates, which is consistent with the previous description.

To further confirm the microstructure of $Ge_{1-x}Mn_x$ FMS, high-resolution transmission electron microscope (HRTEM) measurements were performed for $Ge_{1-x}Mn_x$ FMS at $x = 0.027$, 0.05, and 0.1, respectively. The HRTEM images indicate that $Ge_{1-x}Mn_x$ FMSs are polycrystalline and have a fcc structure with a preferred (111) orientation, as shown in Figs. 2(d) to 2(f). Although single-crystal $Ge_{1-x}Mn_x$ FMS might be obtained by further improving T_R, too high T_R also increases the probability of forming intermetallic precipitates. After careful examination of the zoomed-in images, we did not find the existence of intermetallic precipitates in $Ge_{1-x}Mn_x$ FMS. These results are consistent with the XRD results. According to the inverse fast Fourier transform operation, the interplanar spacings ($d_{\{111\}}$) of $Ge_{1-x}Mn_x$ FMSs are 0.3288, 0.3306, and 0.3311 nm at $x = 0.027$, 0.05, and 0.1, respectively, which is larger than the pure Ge of 0.3264 nm [31]. The deduced a are 0.5695, 0.5726, and 0.5734 nm at $x = 0.027$, 0.05, and 0.1, respectively. Although this result is

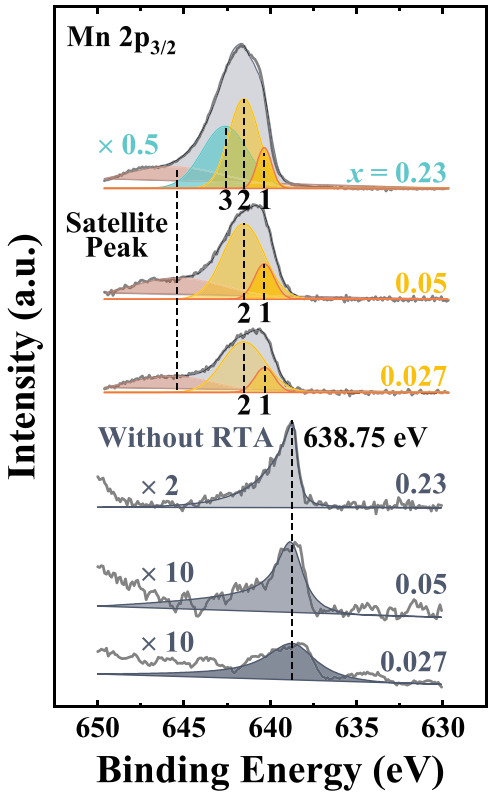

FIG. 3. The XPS spectra with the Lorentzian-Gaussian fitting of Mn $2p_{3/2}$ for different $Ge_{1-x}Mn_x$ films at $x = 0.027$, 0.05, and 0.23, respectively.

not entirely consistent with the XRD result quantitatively, it qualitatively reveals that a indeed increases with x. Both TEM and XRD results indicate that Mn atoms are doped into the Ge host, making the Ge lattice expand.

Furthermore, x-ray photoelectron spectroscopy (XPS) was used to investigate the Mn chemical states in $Ge_{1-x}Mn_x$ films, because the valence state of Mn is related to the microstructures of $Ge_{1-x}Mn_x$ films. Figure 3 presents the XPS spectra with the Lorentzian-Gaussian fitting of Mn $2p_{3/2}$ for different $Ge_{1-x}Mn_x$ films. The Mn $2p_{3/2}$ peaks of amorphous $Ge_{1-x}Mn_x$ (without RTA) at $x = 0.027$, 0.05, and 0.23 are both around 638.75 eV, which is consistent with the previously reported Mn $2p_{3/2}$ peak for Mn metal at 638.64 eV [32], indicating only the Mn^{0+} in amorphous $Ge_{1-x}Mn_x$. Amorphous $Ge_{1-x}Mn_x$ deposited at 50 °C neither crystallizes nor forms intermetallic precipitates. However, for $Ge_{1-x}Mn_x$ FMSs at $x = 0.027$ and 0.05, the Mn $2p_{3/2}$ peaks increase to approximately 641.15 eV and could be decomposed into two peaks at 640.34 eV (peak 1) and 641.57 eV (peak 2). The two peaks correspond to the Mn $2p_{3/2}$ multiple peaks of Mn^{2+} in MnO [32] or (Ga, Mn)As [33] reported at 640.30 and 641.50 eV, indicating that some Mn atoms in $Ge_{1-x}Mn_x$ FMS are Mn^{2+}. The left peaks correspond to the satellite peak of Mn^{2+}, as previously reported [32,33]. These Mn^{2+} correspond to the Mn atoms doped into the Ge host. With further increase in x to 0.23 for $Ge_{1-x}Mn_x$ with intermetallic precipitates, the Mn $2p_{3/2}$ peak increases to 641.87 eV and an additional peak 3 appears at 642.56 eV, attributed to the contribution from the Mn $2p_{3/2}$ multiple peak for Mn^{4+} of 642.50 eV [32,33]. It suggests that both Mn^{2+} and Mn^{4+} are present in $Ge_{1-x}Mn_x$ with intermetallic precipitates; the latter correspond to intermetallic precipitates, consistent with the report of overdoped $Si_{0.25}Ge_{0.75}$: Mn_x FMS [23]. While collecting the XPS spectra of Mn $2p$, the XPS spectra of Mn $3s$ were also collected to aid in distinguishing the valence states of Mn (see the Supplemental Material [27]). The Mn $3s$ peaks of $Ge_{1-x}Mn_x$ FMS exhibit only a splitting amplitude ΔE_1 of 6.2 eV, indicating the presence of Mn^{2+}[34]. In contrast, the Mn $3s$ peaks of $Ge_{1-x}Mn_x$ with intermetallic precipitates exhibit ΔE_1 of 6.2 eV and ΔE_2 of 5 eV, suggesting the presence of Mn^{2+} and Mn^{4+}, respectively [34]. These results summarized from the XPS spectra of Mn $2p$ and $3s$ were consistent.

Combining XRD, HRTEM, and XPS, we believe that our $Ge_{1-x}Mn_x$ FMSs are high-quality FMSs without intermetallic precipitates. Some Mn atoms at interstitial sites replace Ge atoms to the substitutional sites, which will provide both holes and magnetic moments in $Ge_{1-x}Mn_x$ FMS [8,9,35]. The carriers of our $Ge_{1-x}Mn_x$ FMS are indeed holes (Fig. S4 [27]).

B. Magnetic properties

Next, the magnetic properties of $Ge_{1-x}Mn_x$ films at different x were investigated. The temperature dependence of magnetization for representative $Ge_{1-x}Mn_x$ films is shown in Fig. 4(a). These curves were obtained by cooling samples to 10 K with an in-plane field (1 T) and measuring samples to 350 K with a fixed in-plane field (10 mT). These arrows point to T_C extracted by the differentiation of magnetization vs temperature curves (see the Supplemental Material [27]). T_C of $Ge_{1-x}Mn_x$ FMS first increases rapidly from 45 K with $x \leqslant 0.03$ to 266 K at $x = 0.05$ and then is maintained around 280 K with x, as shown in Fig. 4(b). T_C reaches up to 282 K at $x = 0.07$. The increase in x not only provides more magnetic moments but also more hole carriers, both of which play an important role in enhancing hole-mediated ferromagnetism [8,9], thereby increasing T_C. The hole-carrier concentration of $Ge_{1-x}Mn_x$ FMS indeed increases with increasing x (Fig. S5 [27]).

The typical in-plane hysteresis loops at 10 K for representative $Ge_{1-x}Mn_x$ films are plotted in Fig. 4(c). As x increases, the hysteresis of these curves becomes more pronounced. The coercive field ($\mu_0 H_C$) and saturation magnetization (M_S) of $Ge_{1-x}Mn_x$ FMSs at different x are extracted by hysteresis loops. The $\mu_0 H_C$ increases rapidly from ≈ 30 mT with $x \leqslant 0.03$ to ≈ 290 mT with $x > 0.03$, as shown in Fig. 4(d). The M_S also increases quickly with x. Subsequently, we calculated the magnetic moment (m) per Mn atom in $Ge_{1-x}Mn_x$ FMS based on M_S, as shown in Fig. S6 [27]. The m increases first and then decreases with x, with the maximum of 0.80 μ_B/Mn appearing at $x = 0.07$. This result deviates from the theoretical value of 3 μ_B/Mn for Mn atom in Ge film [13], indicating that at most 27% of Mn atoms are magnetically activated and the rest of Mn atoms are paramagnetic. The increase in m with $x \leqslant 0.07$ might be attributed to the enhancement of ferromagnetic interactions with increasing x, while the decrease in m is likely due to the more Mn atoms with $x > 0.07$ that cannot work. We have also noticed that T_C, M_S, and a increase with x and tend to saturate around $x = 0.07$. It is

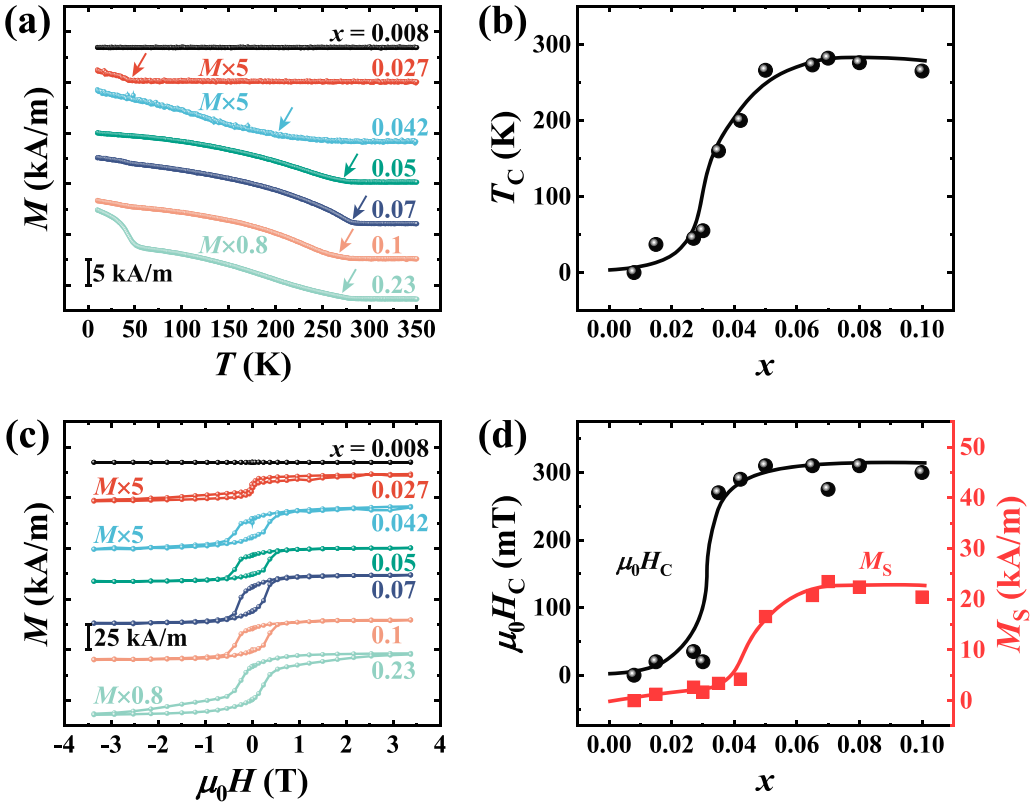

FIG. 4. (a) The temperature dependence of the magnetization with different x under 10 mT. These arrows point to T_C. (b) The x dependence of T_C for $Ge_{1-x}Mn_x$ FMS. (c) The in-plane hysteresis loops with different x at 10 K. (d) The x dependence of $\mu_0 H_C$ and M_S for $Ge_{1-x}Mn_x$ FMS.

not a coincidence, but is closely related to the microstructure. This is likely due to the fact that Mn atoms doped into the Ge host when $x = 0.07$ have approached the limit of their solubility in Ge under the nonequilibrium condition of RTA. When x exceeds 0.07, even more Mn atoms are no longer able to be effectively incorporated into the Ge host and become magnetically activated. This pulls down the calculated average magnetic moment m per Mn atom.

The magnetic properties of $Ge_{1-x}Mn_x$ FMS are significantly different at $x \leqslant 0.03$ and $x > 0.03$. There should be differences in the origin of magnetic properties, even if their microstructures are similar between $x \leqslant 0.03$ and $x > 0.03$. For $Ge_{1-x}Mn_x$ film at $x = 0.008$, it is not ferromagnetic due to its extremely small x. When $0.015 \leqslant x \leqslant 0.03$, T_C are around 45 K, which is low, and $\mu_0 H_C$ are also significantly small compared to $Ge_{1-x}Mn_x$ FMS with $x > 0.03$. The magnetic properties do not seem to originate from long-range hole-mediated ferromagnetism, but are more likely derived from the magnetic moments of individual Mn-rich regions [36,37] illustrated in Fig. 1(e). Fewer Mn atoms in Mn-poor regions, which are mostly not magnetically activated, would result in many Mn-poor regions being paramagnetic. It limits the establishment of ferromagnetic order across the entire film. Therefore, the magnetic properties are still hole mediated but short range. However, as x increases, the $\mu_0 H_C$ (or magnetic hysteresis) becomes significantly large, indicating long-range ferromagnetism. It is likely that the increasing x reduces the number of paramagnetic Mn-poor regions, promoting the formation of long-range hole-mediated ferromagnetism. Although there might still be a few Mn-poor regions that are paramagnetic, it is not enough to prevent the establishment of ferromagnetic order across the entire film. Benefiting from this transformation, T_C and $\mu_0 H_C$ increase rapidly with x, as well as M_S.

As x increases further, the magnetic properties of $Ge_{1-x}Mn_x$ with intermetallic precipitates become distinct from those of $Ge_{1-x}Mn_x$ FMS, as do the electrical transport properties discussed later. For $Ge_{1-x}Mn_x$ with intermetallic precipitates at $x = 0.23$, the M vs T curve shows a significant turning point at low temperature, and the M vs $\mu_0 H$ curve exhibits a large and unique magnetic hysteresis. The magnetic hysteresis loop can be decomposed into two compositions; one is consistent with $Ge_{1-x}Mn_x$ FMS with $x \leqslant 0.1$, attributed to the contribution from $Ge_{1-x}Mn_x$ FMS component. And, the other one with a larger magnetic hysteresis is due to the dispersed intermetallic precipitates in $Ge_{1-x}Mn_x$ film, which might originate from the blocking of intermetallic moments at low temperature. The turning point in the M vs T curve might arise from the blocking temperature or as a result of the formation of coherent intermetallic precipitates causing a metastable state [21]. Of course, a more accurate explanation for the magnetic properties of $Ge_{1-x}Mn_x$ with intermetallic precipitates needs further systematic investigations.

C. Electrical transport properties

Finally, we studied the electrical transport properties of representative $Ge_{1-x}Mn_x$ FMS and $Ge_{1-x}Mn_x$ with

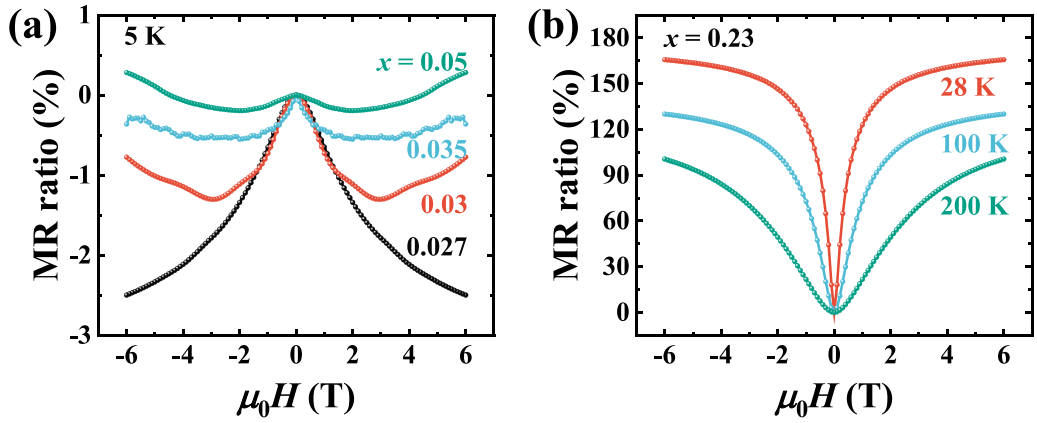

FIG. 5. (a) The MR ratio vs $\mu_0 H$ curves with various x at 5 K. (b) The MR ratio vs $\mu_0 H$ curves with $x = 0.23$ at different temperatures.

intermetallic precipitates, respectively. Figure 5(a) shows MR curves at 5 K for $Ge_{1-x}Mn_x$ FMSs with different x, and the MR ratio decreases with x. In $Ge_{1-x}Mn_x$ FMSs, there are two contributions: negative MR and positive MR. Usually, the negative MR is attributed to spin-dependent scattering of carriers [38], a typical feature of FMSs [3,18,19]. However, as x increases and the ferromagnetism enhances, this negative MR does not increase but instead decreases. Therefore, there should be other mechanisms responsible for the negative MR of $Ge_{1-x}Mn_x$ FMS at low temperature, which is enhanced by an inversely x-correlated physical quantity. This might be due to the orbital weak-localization effect, which also causes negative MR under external magnetic fields, as previously reported [39,40]. With the decrease of x, the hole-carrier concentration decreases (Fig. S5(b) [27]), possibly leading to earlier entry of hole carriers into the orbital weak localization at low temperature, ultimately resulting in the increase of negative MR for $Ge_{1-x}Mn_x$ FMS with decreasing x at 5 K. The positive MR is geometric MR stemming from the Lorentz force, which acts on moving charge carriers [17,28]. This positive MR increases with increasing x, leading to the decrease of the MR ratio for $Ge_{1-x}Mn_x$ FMS.

As x further increases and intermetallic precipitates appear, the electrical transport characteristics become unusual. The positive MR shows a significant enhancement and the MR ratio reaches up to 165% at 28 K under 6 T, as shown in Fig. 5(b). This is significantly higher than the MR ratio of $Ge_{1-x}Mn_x$ FMS without intermetallic precipitates by two orders of magnitude. This enhanced positive MR is only observed in $Ge_{1-x}Mn_x$ with intermetallic precipitates, which is similar to the large geometric MR reported in $Hg_{1-x}Cd_xTe$ [41], $Ag_{2+\delta}Te$, and $Ag_{2+\delta}Se$ [42] with inhomogeneities. As previously mentioned, geometric MR depends on the effect of the Lorentz force, which is canceled out by the Hall potential accumulated at the edges of Hall bar devices. Therefore, shorting out the Hall potential can effectively increase geometric MR, such as Corbino geometry, which is most effective in this regard. Incorporating shorting bars of high-conductivity materials into devices can also effectively short out the Hall potential [43]. In fact, high-conductivity inhomogeneities in semiconductors play a similar role. With increasing x, for $Ge_{1-x}Mn_x$ FMS, the number of relatively high-conductivity Mn-rich regions increases, as illustrated in Fig. 1(e), thus leading to an increase in geometric MR. The conductivity of Mn-rich regions is higher than that of Mn-poor regions, which can be indirectly inferred from the decreasing trend of resistivity with increasing x (Fig. S5(a) [27]). For $Ge_{1-x}Mn_x$ with intermetallic precipitates, the conductivity of intermetallic precipitates should be significantly higher and more effectively short out the Hall potential, thus greatly enhancing geometric MR compared to $Ge_{1-x}Mn_x$ FMS.

Therefore, the MR characteristics change from the small negative MR of $Ge_{1-x}Mn_x$ FMS to the significantly enhanced positive MR of $Ge_{1-x}Mn_x$ with intermetallic precipitates, as illustrated by the curved dashed line with arrows in Fig. 1(e). In fact, the electrical transport characteristics at different x can provide an easy method to distinguish different microstructures in $Ge_{1-x}Mn_x$ films.

D. Discussion

The high-quality FMSs with high T_C but no intermetallic precipitates have always been an important topic in the field of spintronics. However, while preparing FMSs, not only do TM atoms get incorporated into the semiconductor host, but intermetallic precipitates also occur. The formation of both FMSs and intermetallic precipitates depends on two processes: the aggregation of atoms and the formation of solid solutions or intermetallic compounds under sufficient thermal activation energy ($k_B T$). Here, k_B is the Boltzmann constant. For example, the formation of Ge_3Mn_5 intermetallic compounds requires the aggregation of Mn atoms. It relies on either the diffusion of Mn atoms on Ge surface with the barrier energy E_D during the deposition, or the movement of Mn atoms in Ge film with the barrier energy E_M in the postannealing process, as illustrated in Figs. 6(a) and 6(b), respectively. In fact, the formation of $Ge_{1-x}Mn_x$ FMS is not influenced by this process, as there are plenty of Ge atoms surrounding Mn atoms in the Ge host. Therefore, we focus on strategies to suppress intermetallic precipitates by carefully considering the energetics or spatial distribution of Mn atoms.

Figure 6(c) illustrates the second process of the formation of $Ge_{1-x}Mn_x$ FMS and intermetallic precipitates, which could lower the total energy from E_0 (ground state) to E_1 and E_2 with an energy barrier E_B. These processes and their priorities are governed by different energies involved, i.e., the forming

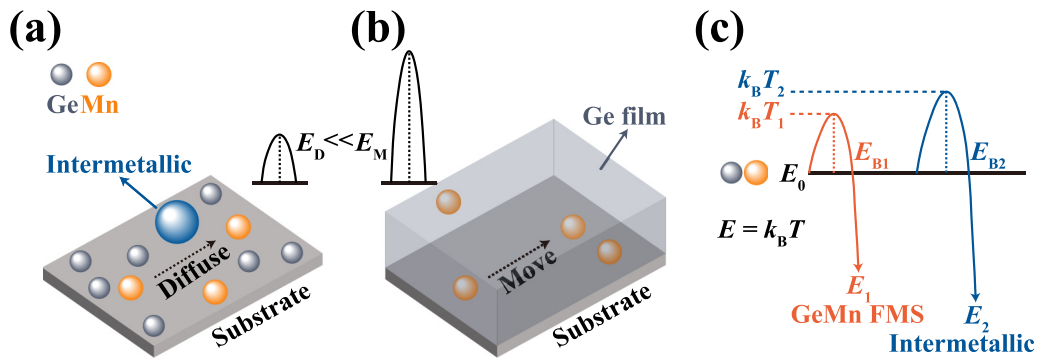

FIG. 6. (a) The diffusion of Mn atoms on Ge surface with the barrier energy E_D during the deposition. (b) The movement of Mn atoms in Ge film with the barrier energy E_M in the postannealing process. (c) This schematic diagram illustrates that Mn atoms overcome E_{B1} and E_{B2} to form $Ge_{1-x}Mn_x$ FMS and intermetallic precipitates, respectively.

energy $E_1(E_2)$, the energy barrier $E_{B1}(E_{B2})$, and the thermal activation energy k_BT. The fact of formation of intermetallic precipitates in various conditions at different composition and temperatures [20,44] indicates that it is energetically favored with its E_2 lower than E_1 of $Ge_{1-x}Mn_x$ FMS. It has been theoretically predicted that the strain or high pressure can affect the lattice and lower the forming energy, which could increase the solubility of Mn and suppress the intermetallic phase [45]. However, this method by controlling the forming energy is not industrial friendly and cannot fully avoid intermetallic precipitates in $Ge_{1-x}Mn_x$ films.

The Mn and Ge atoms with sufficient k_BT can overcome E_B to form either $Ge_{1-x}Mn_x$ FMS or intermetallic precipitates, as depicted in Fig. 6(c). During the preparation of $Ge_{1-x}Mn_x$ FMS by MBE at high T_S, Mn atoms not only overcome E_{B1} ($E_{B1} = k_BT_1$) to form $Ge_{1-x}Mn_x$ FMS, but also overcome E_{B2} ($E_{B2} = k_BT_2$) to form intermetallic precipitates. Usually, E_{B2} might be slightly larger than E_{B1}; otherwise, it is hard to form $Ge_{1-x}Mn_x$ FMS under thermal equilibrium once $k_BT > E_{B2}$. In fact, T_1 and T_2 can be as low as 60 °C [21] and 70 ∼ 130 °C [13,17], respectively. The deduced E_{B1} and E_{B2} are 0.029 eV and 0.03 ∼ 0.035 eV, which are quite close. Therefore, it is also difficult to achieve a temperature window to selectively activate the formation of $Ge_{1-x}Mn_x$ FMS and avoid the formation of intermetallic precipitates through their energy barriers.

To effectively suppress the formation of intermetallic precipitates, relying solely on energetics is inadequate. Instead, it is necessary to explore alternative strategies, particularly considering the diluted distribution of Mn atoms in the Ge host. Therefore, preparing $Ge_{1-x}Mn_x$ FMS at low T_S combined with RTA is a promising approach [23], as the aggregation of Mn atoms in Ge film is more challenging than that on Ge surface, given that $E_M >> E_D$ [46–49]. The probability (P) of the diffusion of atoms from one site to the next is $v_0e^{-E_D/k_BT}$, where $v_0 = 1 \times 10^{12}$/s [50]. The probability of Mn atom diffusion on Ge surface during the deposition can be written as $P_D = t_Dv_0e^{-E_D/k_BT_S}$, assuming that $t_D \approx 60$ s (the time for monolayer in MBE), $T_S \approx 60$ °C (the minimum critical temperature for intermetallic precipitates), and $E_D \approx 0.05$ eV [46,47]. For our $Ge_{1-x}Mn_x$ films without RTA, they are amorphous and completely avoid intermetallic precipitates. The Mn atoms are localized in Ge film. The probability of Mn atom movement in Ge film in the RTA process is $P_M = t_{RTA}v_0e^{-E_M/k_BT_R}$, where $t_{RTA} = 30$ s, $T_R = 800$ °C, and E_M is around 1 eV [48,49]. The P_M/P_D is approximately 6×10^{-5}, indicating that the movement and aggregation of Mn atoms in Ge film are indeed restricted. Therefore, the formation of intermetallic precipitates is completely avoided. We have roughly estimated the minimum critical T_R for the appearance of intermetallic precipitates by comparing P_D, which is up to 900 °C. Obviously, 800 °C is large enough to allow Mn atoms to overcome E_{B1}, but also avoids the free movement of Mn atoms in Ge film.

Therefore, depositing film at low T_S combined with a key RTA treatment does perform excellently in the preparation of high-quality $Ge_{1-x}Mn_x$ FMS without intermetallic precipitates. This method significantly extends the window of preparation conditions for $Ge_{1-x}Mn_x$ FMS by suppressing the movement of Mn atoms in Ge film, which can even be further optimized by t_{RTA}. The maximum doping composition has been increased from $x = 0.035$ of $Ge_{1-x}Mn_x$ FMS grown by MBE at slightly higher T_S [13,21] to $x = 0.1$ of $Ge_{1-x}Mn_x$ FMS prepared by this method. Thus, T_C has also been improved from 116 to 282 K. Wang *et al.* have previously prepared $Si_{0.25}Ge_{0.75} : Mn_x$ FMS using a similar method, but T_S was 250 °C [23]. We note that although T_C of $Si_{0.25}Ge_{0.75} : Mn_{0.05}$ FMS can reach 280 K, intermetallic precipitates might exist in film. As we discussed before, intermetallic precipitates in films can result in large MR. The MR ratio of $Si_{0.25}Ge_{0.75} : Mn_{0.025}$ FMS is as high as ≈4000% at 60 K under 6 T, which might be attributed to the shorting effect of intermetallic precipitates on the Hall potential.

IV. CONCLUSION

In conclusion, we prepared high-quality $Ge_{1-x}Mn_x$ FMS without intermetallic precipitates by magnetron sputtering at low T_S combined with a key nonequilibrium RTA treatment. The avoidance of intermetallic precipitates benefits from the suppression of atomic movement in Ge film. This greatly extends the preparation window for $Ge_{1-x}Mn_x$ FMS without intermetallic precipitates. The phase diagram of $Ge_{1-x}Mn_x$

films versus x and T_R was obtained, and face-centered cubic structure $Ge_{1-x}Mn_x$ FMS can be achieved. The maximum Mn doping composition x can reach up to 0.1, which is superior to previous studies. In $Ge_{1-x}Mn_x$ FMS, some Mn atoms replaced Ge atoms from interstitial sites to substitutional sites during the RTA, providing holes and magnetic moments. As x increases, the hole-mediated ferromagnetism of $Ge_{1-x}Mn_x$ FMS is enhanced. T_C also increases with x, up to 282 K at $x = 0.07$. When $x > 0.1$, intermetallic precipitates will inevitably appear in $Ge_{1-x}Mn_x$ films. The MR of $Ge_{1-x}Mn_x$ with intermetallic precipitates is the enhanced positive MR and larger than that of $Ge_{1-x}Mn_x$ FMS by two orders, as intermetallic precipitates effectively short out the Hall potential. Therefore, this characteristic can provide an easy method to confirm high-quality $Ge_{1-x}Mn_x$ FMS. Finally, high-quality $Ge_{1-x}Mn_x$ FMS prepared by suppressing atomic movement in film provided an idea and path for further investigation of ferromagnetic semiconductors.

ACKNOWLEDGMENTS

This work was supported by the Project for Young Scientists in Basic Research of Chinese Academy of Sciences (Grant No. YSBR-030), the National Key R&D Program of China (Grant No. 2021YFA1202200), and the Key Research Project of Frontier Science of Chinese Academy of Sciences (Grants No. XDB44000000 and No. XDB28000000). H.W. also acknowledges the support from the Youth Innovation Promotion Association, Chinese Academy of Sciences (Grant No. 2021110).

[1] T. Dietl, A. Bonanni, and H. Ohno, Families of magnetic semiconductors–an overview, J. Semicond. **40**, 080301 (2019).

[2] H. Ohno, Making nonmagnetic semiconductors ferromagnetic, Science **281**, 951 (1998).

[3] L. Chen, X. Yang, F. Yang, J. Zhao, J. Misuraca, P. Xiong, and S. von Molnár, Enhancing the Curie temperature of ferromagnetic semiconductor (Ga, Mn)As to 200 K via nanostructure engineering, Nano Lett. **11**, 2584 (2011).

[4] H. Wang, J. Ma, and J. Zhao, Giant modulation of magnetism in (Ga,Mn)As ultrathin films via electric field, J. Semicond. **40**, 092501 (2019).

[5] X. Liu, L. Riney, J. Guerra, W. Powers, J. Wang, J. K. Furdyna, and B. A. Assaf, Colossal negative magnetoresistance from hopping in insulating ferromagnetic semiconductors, J. Semicond. **43**, 112502 (2022).

[6] D. Ferrand, J. Cibert, A. Wasiela, C. Bourgognon, S. Tatarenko, G. Fishman, T. Andrearczyk, J. Jaroszyński, S. Koleśnik, T. Dietl, B. Barbara, and D. Dufeu, Carrier-induced ferromagnetism in $p-Zn_{1-x}Mn_xTe$, Phys. Rev. B **63**, 085201 (2001).

[7] M. Venkatesan, C. B. Fitzgerald, J. G. Lunney, and J. M. D. Coey, Anisotropic ferromagnetism in substituted zinc oxide, Phys. Rev. Lett. **93**, 177206 (2004).

[8] T. Dietl, H. Ohno, F. Matsukura, J. Cibert, and D. Ferrand, Zener model description of ferromagnetism in zinc-blende magnetic semiconductors, Science **287**, 1019 (2000).

[9] T. Dietl, H. Ohno, and F. Matsukura, Hole-mediated ferromagnetism in tetrahedrally coordinated semiconductors, Phys. Rev. B **63**, 195205 (2001).

[10] M. Jiang, H. Asahara, S. Sato, T. Kanaki, H. Yamasaki, S. Ohya, and M. Tanaka, Efficient full spin-orbit torque switching in a single layer of a perpendicularly magnetized single-crystalline ferromagnet, Nat. Commun. **10**, 2590 (2019).

[11] Y. Adhikari, T. Liu, H. Wang, Z. Hua, H. Liu, E. Lochner, P. Schlottmann, B. Yan, J. Zhao, and P. Xiong, Interplay of structural chirality, electron spin and topological orbital in chiral molecular spin valves, Nat. Commun. **14**, 5163 (2023).

[12] J. Zhao, F. Matsukura, E. Abe, D. Chiba, Y. Ohno, K. Takamura, and H. Ohno, Growth and properties of (Ga, Mn)As on Si (100) substrate, J. Cryst. Growth **237**, 1349 (2002).

[13] Y. D. Park, A. T. Hanbicki, S. C. Erwin, C. S. Hellberg, J. M. Sullivan, J. E. Mattson, T. F. Ambrose, A. Wilson, G. Spanos, and B. T. Jonker, A group-IV ferromagnetic semiconductor: Mn_xGe_{1-x}, Science **295**, 651 (2002).

[14] K. Murata, C. Kirkham, S. Tsubomatsu, T. Kanazawa, K. Nitta, Y. Terada, T. Uruga, K.-i. Nittoh, D. R. Bowler, and K. Miki, Atomic layer doping of Mn magnetic impurities from surface chains at a Ge/Si hetero-interface, Nanoscale **10**, 295 (2018).

[15] F. Tsui, L. He, L. Ma, A. Tkachuk, Y. S. Chu, K. Nakajima, and T. Chikyow, Novel germanium-based magnetic semiconductors, Phys. Rev. Lett. **91**, 177203 (2003).

[16] H. Braak, R. R. Gareev, D. E. Bürgler, R. Schreiber, P. Grünberg, and C. M. Schneider, Magnetic characteristics of epitaxial Ge(Mn,Fe) diluted films—a new room temperature magnetic semiconductor? J. Magn. Magn. Mater. **286**, 46 (2005).

[17] M. Jamet, A. Barski, T. Devillers, V. Poydenot, R. Dujardin, P. Bayle-Guillemaud, J. Rothman, E. Bellet-Amalric, A. Marty, J. Cibert, R. Mattana, and S. Tatarenko, High-Curie-temperature ferromagnetism in self-organized $Ge_{1-x}Mn_x$ nanocolumns, Nat. Mater. **5**, 653 (2006).

[18] F. Xiu, Y. Wang, K. Wong, Y. Zhou, X. Kou, J. Zou, and K. L. Wang, MnGe magnetic nanocolumns and nanowells, Nanotechnology **21**, 255602 (2010).

[19] T. Nie, X. Kou, J. Tang, Y. Fan, S. Lee, Q. He, L. T. Chang, K. Murata, Y. Gen, and K. L. Wang, Nanoengineering of an Si/MnGe quantum dot superlattice for high Curie-temperature ferromagnetism, Nanoscale **9**, 3086 (2017).

[20] Y. D. Park, A. Wilson, A. T. Hanbicki, J. E. Mattson, T. Ambrose, G. Spanos, and B. T. Jonker, Magnetoresistance of Mn:Ge ferromagnetic nanoclusters in a diluted magnetic semiconductor matrix, Appl. Phys. Lett. **78**, 2739 (2001).

[21] D. Bougeard, S. Ahlers, A. Trampert, N. Sircar, and G. Abstreiter, Clustering in a precipitate-free GeMn magnetic semiconductor, Phys. Rev. Lett. **97**, 237202 (2006).

[22] E. Arras, D. Caliste, T. Deutsch, F. Lancon, and P. Pochet, Phase diagram, structure, and magnetic properties of the Ge-Mn system: A first-principles study, Phys. Rev. B **83**, 174103 (2011).

[23] H. Wang, S. Sun, J. Lu, J. Xu, X. Lv, Y. Peng, X. Zhang, Y. Wang, and G. Xiang, High Curie temperature ferromagnetism

and high hole mobility in tensile strained Mn–doped SiGe thin films, Adv. Funct. Mater. **30**, 2002513 (2020).

[24] W. C. Johnson and G. H. Ridgely, Nitrogen compounds of germanium. V. Germanous nitride, J. Am. Chem. Soc. **56**, 2395 (1934).

[25] M. Mayr, G. Alvarez, and E. Dagotto, Global versus local ferromagnetism in a model for diluted magnetic semiconductors studied with Monte Carlo techniques, Phys. Rev. B **65**, 241202(R) (2002).

[26] X. Wang, H. Wang, D. Pan, L. Li, X. Yu, J. Lu, J. Zhao, T. Keiper, E. Lochner, and S. von Molnár, Robust manipulation of magnetism in dilute magnetic semiconductor (Ga, Mn) As by organic molecules, in *2016 IEEE International Nanoelectronics Conference (INEC)* (IEEE, 2016), pp. 1–3.

[27] See Supplemental Material at http://link.aps.org/supplemental/10.1103/PhysRevB.109.024407 for the differentiation of magnetization vs temperature curve; the XRD patterns of films at different RTA temperatures and growth temperatures; the XPS spectra of Mn 3s; the anomalous Hall-effect curve of FMS; the change of the resistivity and hole-carrier concentration for FMS with x; and the x dependence of the saturation magnetization and magnetic moment per Mn atom in FMS.

[28] Y. K. Wakabayashi, R. Akiyama, Y. Takeda, M. Horio, G. Shibata, S. Sakamoto, Y. Ban, Y. Saitoh, H. Yamagami, A. Fujimori, M. Tanaka, and S. Ohya, Origin of the large positive magnetoresistance of $Ge_{1-x}Mn_x$ granular thin films, Phys. Rev. B **95**, 014417 (2017).

[29] A. Wosylus, Y. Prots, W. Schnelle, M. Hanfland, and U. Schwarz, Crystal structure refinements of Ge (tP12), physical properties and pressure-induced phase transformation Ge (tP12) ↔ Ge (tI4), Z. Naturforsch. B **63**, 608 (2008).

[30] S. Cho, S. Choi, S. C. Hong, Y. Kim, J. B. Ketterson, B.-J. Kim, Y. C. Kim, and J.-H. Jung, Ferromagnetism in Mn-doped Ge, Phys. Rev. B **66**, 033303 (2002).

[31] A. Grytsiv, N. Melnychenko-Koblyuk, N. Nasir, P. Rogl, A. Saccone, and H. Schmid, Formation of clathrates Ba−M − Ge(M = Mn, Fe, Co), Int. J. Mater. Res. **100**, 189 (2009).

[32] M. C. Biesinger, B. P. Payne, A. P. Grosvenor, L. W. Lau, A. R. Gerson, and R. S. C. Smart, Resolving surface chemical states in XPS analysis of first row transition metals, oxides and hydroxides: Cr, Mn, Fe, Co and Ni, Appl. Surf. Sci. **257**, 2717 (2011).

[33] S. A. Hatfield, T. D. Veal, C. F. McConville, G. R. Bell, K. W. Edmonds, R. P. Campion, C. T. Foxon, and B. L. Gallagher, Photoelectron spectroscopy study of $Ga_{1-x}Mn_xAs(001)$ surface oxide and low temperature cleaning, Surf. Sci. **585**, 66 (2005).

[34] L. Zhao, Y. Jiang, J. Hao, H. Wei, W. Zheng, and L. Mao, Graphdiyne oxide enhances the stability of solid contact-based ionselective electrodes for excellent in vivo analysis, Sci. China: Chem. **62**, 1414 (2019).

[35] Y. J. Zhao, T. Shishidou, and A. J. Freeman, Ruderman-Kittel-Kasuya-Yosida-like ferromagnetism in Mn_xGe_{1-x}, Phys. Rev. Lett. **90**, 047204 (2003).

[36] R. Morgunov, M. Farle, M. Passacantando, L. Ottaviano, and O. Kazakova, Electron spin resonance and microwave magnetoresistance in Ge:Mn thin films, Phys. Rev. B **78**, 045206 (2008).

[37] R. B. Morgunov, A. I. Dmitriev, and O. L. Kazakova, Percolation ferromagnetism and spin waves in Ge:Mn thin films, Phys. Rev. B **80**, 085205 (2009).

[38] H. Akinaga, J. De Boeck, G. Borghs, S. Miyanishi, A. Asamitsu, W. Van Roy, Y. Tomioka, and L. H. Kuo, Negative magnetoresistance in GaAs with magnetic MnAs nanoclusters, Appl. Phys. Lett. **72**, 3368 (1998).

[39] F. Matsukura, M. Sawicki, T. Dietl, D. Chiba, and H. Ohno, Magnetotransport properties of metallic (Ga,Mn)As films with compressive and tensile strain, Physica E (Amsterdam, Neth.) **21**, 1032 (2004).

[40] T. Dietl, Interplay between carrier localization and magnetism in diluted magnetic and ferromagnetic semiconductors, J. Phys. Soc. Jpn. **77**, 031005 (2008).

[41] T. Thio and S. A. Solin, Giant magnetoresistance enhancement in inhomogeneous semiconductors, Appl. Phys. Lett. **72**, 3497 (1998).

[42] R. Xu, A. Husmann, T. Rosenbaum, M.-L. Saboungi, J. Enderby, and P. Littlewood, Large magnetoresistance in nonmagnetic silver chalcogenides, Nature (London) **390**, 57 (1997).

[43] D. R. Baker and J. P. Heremans, Linear geometrical magnetoresistance effect: Influence of geometry and material composition, Phys. Rev. B **59**, 13927 (1999).

[44] C. Zeng, S. C. Erwin, L. C. Feldman, A. P. Li, R. Jin, Y. Song, J. R. Thompson, and H. H. Weitering, Epitaxial ferromagnetic Mn_5Ge_3 on Ge(111), Appl. Phys. Lett. **83**, 5002 (2003).

[45] D. A. Cogswell and M. Z. Bazant, Coherency strain and the kinetics of phase separation in $LiFePO_4$ nanoparticles, ACS Nano **6**, 2215 (2012).

[46] T. Hama, K. Kuwahata, N. Watanabe, A. Kouchi, Y. Kimura, T. Chigai, and V. Pirronello, The mechanism of surface diffusion of H and D atoms on amorphous solid water: Existence of various potential sites, Astrophys. J. **757**, 185 (2012).

[47] H. Brune, K. Bromann, H. Röder, K. Kern, J. Jacobsen, P. Stoltze, K. Jacobsen, and J. Norskov, Effect of strain on surface diffusion and nucleation, Phys. Rev. B **52**, R14380(R) (1995).

[48] A. Portavoce, O. Abbes, Y. Rudzevich, L. Chow, V. Le Thanh, and C. Girardeaux, Manganese diffusion in monocrystalline germanium, Scr. Mater. **67**, 269 (2012).

[49] E. N. Sgourou, Y. Panayiotatos, R. V. Vovk, N. Kuganathan, and A. Chroneos, Diffusion and dopant activation in germanium: Insights from recent experimental and theoretical results, Appl. Sci. **9**, 2454 (2019).

[50] D. H. Wei, C. L. Gao, K. Zakeri, and M. Przybylski, Pd atomic chain formation as a result of submonolayer deposition of 3*d* metals on Pd(110), Phys. Rev. Lett. **103**, 225504 (2009).